FRONTIERS OF PHYSICS

VIEW & PERSPECTIVE
Volume 19 / Issue 2 / 24301 / 2024

A semiclassical perspective on nuclear chirality

Radu Budaca[1,2]

1 "Horia Hulubei" National Institute for R&D in Physics and Nuclear Engineering, Str. Reactorului 30, RO- 077125, POB-MG6 Bucharest-Măgurele, Romania
2 Academy of Romanian Scientists, Splaiul Independenței 54, 050044, Bucharest, Romania
Corresponding author. E-mail: rbudaca@theory.nipne.ro
Received February 1, 2023; accepted August 8, 2023

ABSTRACT

The application of the semiclassical description to a particle-core system with imbued chiral symmetry is presented. The classical features of the chiral geometry in atomic nuclei and the associated dynamics are investigated for various core deformations and single-particle alignments. Distinct dynamical characteristics are identified in specific angular momentum ranges, triaxiality and alignment conditions. Quantum observables will be extracted from the classical picture for a quantitative description of experimental data provided as numerical examples of the model's performance.

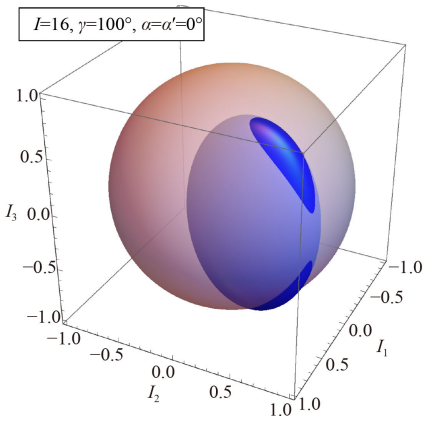

Keywords chiral symmetry, triaxial nuclei, semiclassical description

1 Introduction

Chirality or handedness is an ever-present motive in nature. Geometrical configurations related through a space inversion regularly occur in optics, chemistry, particle physics and even macroscopic biological ensembles such as spirals, shells, and hands. In nuclear physics, chirality is associated with the geometry of three mutually perpendicular angular momenta which can form a righthanded and a lefthanded trihedron. It is therefore of a dynamical character, the two configurations being related through a rotation and a time reversal transformation. This particular arrangement emerges in triaxial nuclei, where the three perpendicular angular momentum vectors are associated with the core rotation, and the orbits of two or more quasiparticles from opposite extremes of their valence orbitals [1]. In the laboratory frame of reference, the two systems of opposite chirality are indistinguishable, such that one expects to observe a degenerated doublet of bands with $\Delta I = 1$ and the same parity [2]. Since its prediction [1] and experimental confirmation [3], nuclear chirality became the focus of numerous experimental and theoretical studies. Its manifestation is now spread in over several dozens of nuclei [4–10], combining presently other various nuclear structure effects [11–14]. The theoretical interpretation of the experimental data in terms of the chiral geometry of the involved angular momentum vectors is traditionally based on expectation values of orientation observables calculated within diverse versions and extensions [8, 15–22] of the Particle Rotor Model (PRM) [23] or using projected [24–29] or cranked mean-filed [30–37] formalisms. The semiclassical treatment of the system which has the chiral symmetry as a starting hypothesis is an alternative theoretical approach [7, 38–41]. In this study an extensive review of the semiclassical procedure will be presented, followed by a detailed analysis of the classical dynamics of nuclear chirality as a function of deformation and alignment configuration. For practical applications, one will also show how to extract quantum

*Special Topic: Nuclear Chirality over the Past 25 Years (Eds. Qibo Chen & Pengwei Zhao).

Higher Education Press

https://doi.org/10.1007/s11467-023-1339-6

observables from the obtained classical picture and calculate them for few demonstrative examples.

2 Semiclassical formalism

The PRM Hamiltonian for a total angular momentum $\hat{\boldsymbol{I}}$ of a system composed of a triaxially deformed core and two particles with spins $\boldsymbol{j}$ and $\boldsymbol{j}'$ [23] is just a sum of the terms corresponding to the specific degrees of freedom

$$H = H_R + H_{qp} + H'_{qp}. \tag{2.1}$$

Thus, the triaxial rotor part of the total Hamiltonian

$$H_R = \sum_{k=1,2,3} A_k(\hat{I}_k - \hat{j}_k - \hat{j'}_k)^2 \tag{2.2}$$

describes the core rotation in terms of its angular momentum $\boldsymbol{R} = \boldsymbol{I} - \boldsymbol{j} - \boldsymbol{j}'$ and involves inertial parameters $A_k = 1/(2\mathcal{J}_k)$. Here, the moments of inertia (MOI) along the body-fixed principal axes which define A_k are given by the hydrodynamic nuclear model [23]:

$$\mathcal{J}_k = \frac{4}{3}\mathcal{J}_0 \sin^2\left(\gamma - \frac{2}{3}k\pi\right). \tag{2.3}$$

In the same representation, the direction of the total angular momentum vector relative to the density distribution can be tracked by referring to axes 1, 2 and 3 as the long (l), short (s) and medium (m), respectively, which designates the relationship between the corresponding semi-axes of the nuclear ellipsoid when $\gamma \in (60°, 120°)$. The core will favor then rotation around the m-axis, while a hole(particle)-type quasiparticle will execute orbits around the $l(s)$-axis [1].

In what follows, one will consider that the spins of the quasiparticles are rigidly aligned relative to the intrinsic frame of reference with small deviations from the perfect trihedral geometry. Then the rigid or frozen alignment (FA) is expressed as

$$\begin{aligned}
&\hat{j}_1 = j_1\cos\alpha,\ \hat{j'}_1 = 0,\\
&\hat{j}_2 = 0,\ \hat{j'}_2 = j'\cos\alpha',\\
&\hat{j}_3 = j\sin\alpha,\ \hat{j'}_3 = j'\sin\alpha',
\end{aligned} \tag{2.4}$$

where the quasiparticle spin operators are replaced with real numbers associated with their expectation values. As the two quasiparticle spins are rigidly aligned along the principal planes 1-3 and 2-3, α and α' angles account for their deviation in respect to the l and s axes. The relevant part of the particle-rotor Hamiltonian within this approximation is reduced by removing the constant quasiparticle contribution to

$$\begin{aligned}
H_{chiral} =& A_1\hat{I}_1^2 + A_2\hat{I}_2^2 + A_3\hat{I}_3^2\\
&- 2A_1 j\hat{I}_1\cos\alpha - 2A_2 j'\hat{I}_2\cos\alpha'\\
&- 2A_3(j\sin\alpha + j'\sin\alpha')\hat{I}_3.
\end{aligned} \tag{2.5}$$

This operator is nothing else than a cranked rotor Hamiltonian for a total spin $\hat{I}$, which remains the only active operator. It is important to mention that the D_2 octahedral symmetry of the triaxial core [23] is conserved by the invariance of (2.5) to the change $\hat{I}_k(j_k, j'_k) \to -\hat{I}_k(-j_k, -j'_k)$. Such second order polynomials in angular momentum components are standard Hamiltonian objects in the classical mechanics of rigid body dynamics [42, 43], and were also considered for few quantum nuclear systems [44, 45].

For a semiclassical investigation of the rotational motion described by the quantum Hamiltonian (2.5), a time-dependent variational principle [46] is considered with an angular momentum coherent state as a variational function. Its expansion in eigenfunctions of the total angular momentum operator, and its projections on the third intrinsic (K) and laboratory (M) principal axis $|IMK\rangle$ can be expressed as

$$\begin{aligned}
|\psi_{IM}(\theta,\varphi)\rangle =& \sum_{K=-I}^{I}\frac{1}{2^I}\sqrt{\frac{(2I)!}{(I-K)!(I+K)!}}\\
&\times(1+\cos\theta)^{\frac{I-K}{2}}(1-\cos\theta)^{\frac{I+K}{2}}\mathrm{e}^{\mathrm{i}\varphi(I+K)}|IMK\rangle.
\end{aligned} \tag{2.6}$$

The variational state is stereographically parametrized by the azimuth and polar angles (φ and θ) determining the direction of the total angular momentum vector. Solving the variational equations, leads to a classical energy function defined as the average of the quantum Hamiltonian on state (2.6) and a couple of equations of motion for φ and θ. Introducing the variable $x = I\cos\theta$, the classical energy function acquires the expression

$$\begin{aligned}
\mathcal{H}(x,\varphi) =& \frac{I}{2}(A_1 + A_2) + A_3 I^2\\
&+ \frac{(2I-1)(I^2-x^2)}{2I}(A_1\cos^2\varphi + A_2\sin^2\varphi - A_3)\\
&- 2\sqrt{I^2-x^2}(A_1 j\cos\alpha\cos\varphi + A_2 j'\cos\alpha'\sin\varphi)\\
&- 2A_3 x(j\sin\alpha + j'\sin\alpha'),
\end{aligned} \tag{2.7}$$

while the equations of motion are brought to a Hamilton canonical form expressed with the help of Poisson bracket as:

$$\{\mathcal{H}, x\} = \dot{x},\ \ \{\mathcal{H}, \varphi\} = \dot{\varphi}. \tag{2.8}$$

This allows the identification of x with the generalized momentum and φ with the generalized coordinate, having the relationship $\{\varphi, x\} = 1$. The new variable x is just the total angular momentum projection on the third intrinsic axis, and it will be referred to as the chiral

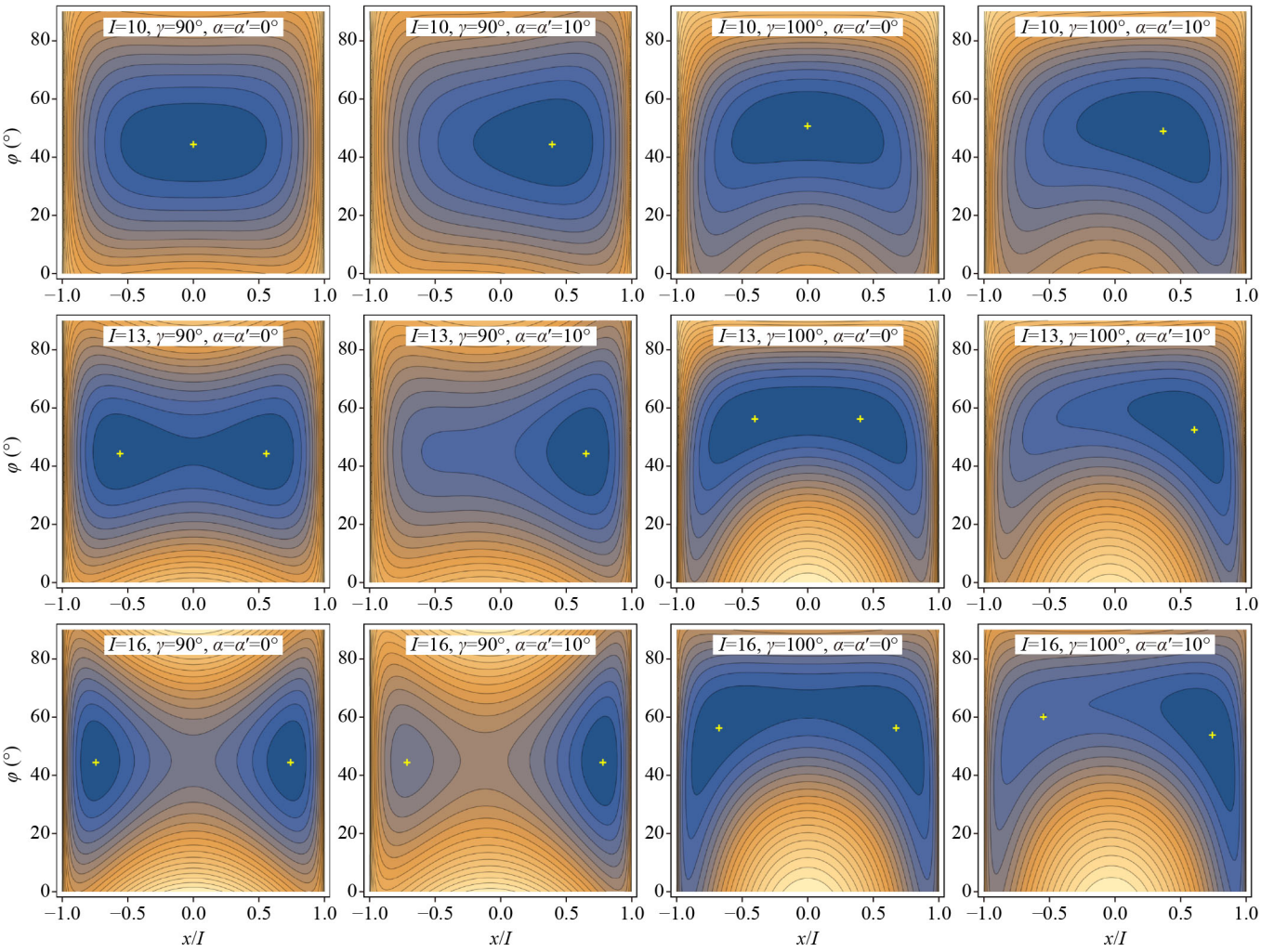

Fig. 1 Classical energy surfaces for $j = j' = 11/2$ and $I = 10, 13, 16$ values of total angular momentum, as a function of φ and the normalized chiral variable x/I, when $\gamma = 90°$, $\alpha = \alpha' = 0$ (first column), $\gamma = 90°$, $\alpha = \alpha' = 10°$ (second column), $\gamma = 100°$, $\alpha = \alpha' = 0°$ (third column), and $\gamma = 100°$, $\alpha = \alpha' = 10°$ (last column). The single or double minima are indicated with crosses.

variable because its sign can be associated with system's chirality.

Few samples of the classical energy function are shown in Fig. 1, which present a common evolution with total angular momentum from a single minimum to a double minimum structure. The dynamical aspects of these two distinct phases will become clear form the following section. Before that, it is worth to mention that the non-vanishing tilting of the quasiparticle spins breaks the $\pm x$ symmetry of the classical energy, while the departure from the maximal triaxiality breaks its symmetry in respect to the $\varphi = 45°$ direction. Moreover, both tilting and triaxiality influence the angular momentum value where the two minima emerge. For the favored case when $j = j' = 11/2$, the departure form the symmetry line $\varphi = 45°$ is identical for the prolate ($\gamma > 90°$) and oblate ($\gamma < 90°$) branches. For different particle and hole spin alignments, the two situations will differ. Nevertheless, for prolate shapes the minima come closer to the short principal axis ($\varphi_m > 45°$), while for the oblate ones they move towards the long principal axis ($\varphi_m < 45°$). Similarly, the $\varphi = 45°$ symmetry axis for $\gamma = 90°$ will move towards the principal axis with the larger quasiparticle alignment.

3 Classical dynamics

The canonical coordinates of the classical energy minima designate the average direction of the total angular momentum vector. Their evolution with spin for distinct triaxiality and alignment conditions is shown in Fig. 2.

In the absence of tilting, the coordinates of the minima acquire closed analytical expressions divided into two phases by a critical angular momentum I_c marking the doubling of the minimum points. Thus, for $I < I_c$ one obtains $x_p = 0$ and a quartic equation for $\sin\varphi_p$:

$$\frac{2I-1}{2}(A_2-A_1)\cos\varphi_p\sin\varphi_p = A_2 j'\cos\varphi_p - A_1 j\sin\varphi_p. \tag{3.1}$$

Note that the average direction of the total angular momentum vector for this solution resides in the principal plane 1–2 defined by the quasiparticle alignments. This is the classical equivalent of the planar (p) solution from the TAC calculations of Ref. [1]. Consequently, for $I > I_c$ one obtains the aplanar (a) solution [1] which provides a constant azimuth angle coordinate

$$\tan\varphi_a = \frac{A_2 j'(A_1-A_3)}{A_1 j(A_2-A_3)}, \tag{3.2}$$

and two angular momentum dependent solutions for the chiral variable $x_a = \pm I\cos\theta_a^I$, where

$$\sin\theta_a^I = \frac{2\sqrt{A_1^2 j^2(A_2-A_3)^2 + A_2^2 j'^2(A_1-A_3)^2}}{(2I-1)(A_1-A_3)(A_2-A_3)}. \tag{3.3}$$

These two aplanar solutions represent orientations of the total angular momentum vector with opposite handedness in respect to the intrinsic reference frame. Eq. (3.3) for $\sin\theta_a^I = 1$ provides also an analytical expression for the critical angular momentum marking the splitting of the minimum:

$$I_c = \frac{\sqrt{A_1^2 j^2(A_2-A_3)^2 + A_2^2 j'^2(A_1-A_3)^2}}{(A_1-A_3)(A_2-A_3)} + \frac{1}{2}. \tag{3.4}$$

Figure 3 shows that it has a parabolic-like dependence on triaxiality. It is symmetrical in respect to the $\gamma = 90°$ value due to equal alignments $j = j'$, otherwise, the prolate and oblate branches will be distinct [38].

Allowing a non-vanishing tilting of the quasiparticle alignments induces important changes to the simple picture described above. First of all, the two minima generated above I_c have from the start a very large separation in respect to x variable [Fig. 2(b)], instead of a smooth increase [Fig. 2(a)] found for the principal axes alignments. In what concerns the azimuth coordinate of the minima, one can see from Fig. 2(c) that it keeps its general evolution with spin but is no longer fractured in distinct phases. Indeed its discontinuity at the critical point I_c when $\gamma \neq 90°$, is smoothed out by the tilting of the quasiparticle spins. The effect of the tilting on the $\gamma = 90°$ case resumes to the shifting of the constant φ_m to higher values for $\alpha > \alpha'$, and respectively to lower values for $\alpha < \alpha'$, otherwise the $\varphi_m = const.$ is invariant for any $\alpha = \alpha'$. The critical angular momentum I_c is raised by the tilted alignments. Although it keeps its parabolic-like dependence on triaxiality shown in Fig. 3, it has a sharper minimum at $\gamma = 90°$, making thus the associated dynamics more sensible to small deviation from the maximal triaxiality.

It is important to mention that the analytical proceedings even for non-vanishing tilting are greatly simplified for the special case of maximum triaxiality

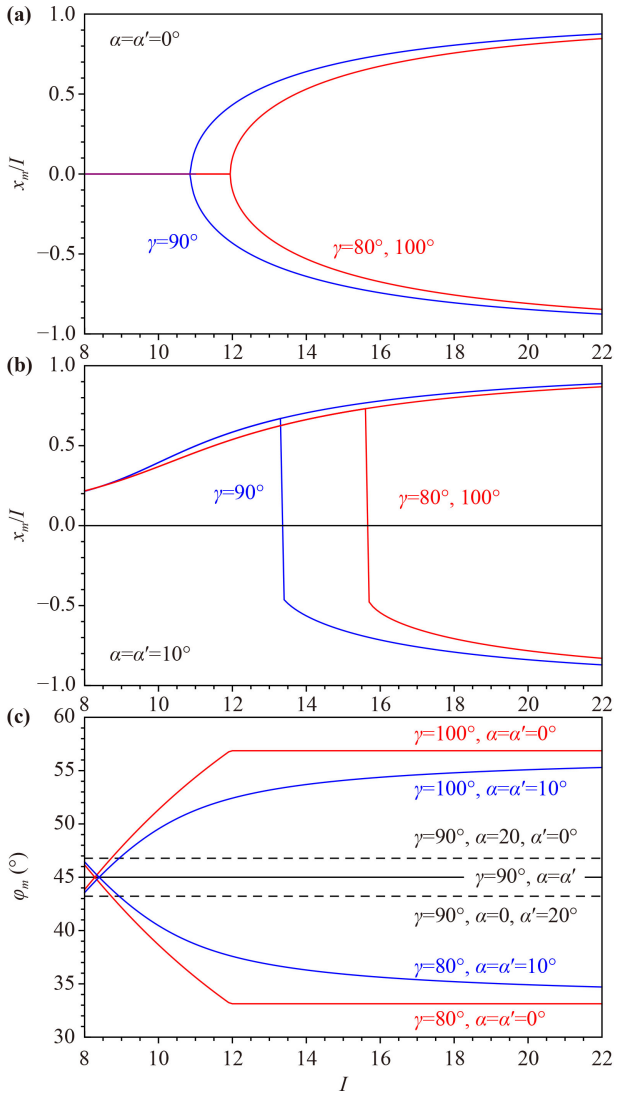

Fig. 2 Evolution with angular momentum of the chiral coordinate for the classical energy minima in the absence **(a)** and presence of tilting **(b)**. The corresponding dependence on angular momentum of the azimuth coordinate of the classical energy minima is shown in panel **(c)**.

$\gamma = 90°$, where $A_1 = A_2$. In this case the azimuth coordinate of the minima is simply given as $\tan\varphi_m = \frac{j'\cos\alpha'}{j\cos\alpha}$ and remains spin independent regardless of the tilting as can be attested by the graph of Fig. 2(c).

The stationary points of the classical energy function which are minima in Fig. 1 correspond to stable dynamical configurations. The classical orbits of the total angular momentum vector are constructed around these stationary points and follow the constant energy contours. A more intuitive visualization of the classical trajectories can be accomplished within the space of the classical components of the total angular momentum defined as expectation values of the operators for the angular momentum projections on the variational state (2.6):

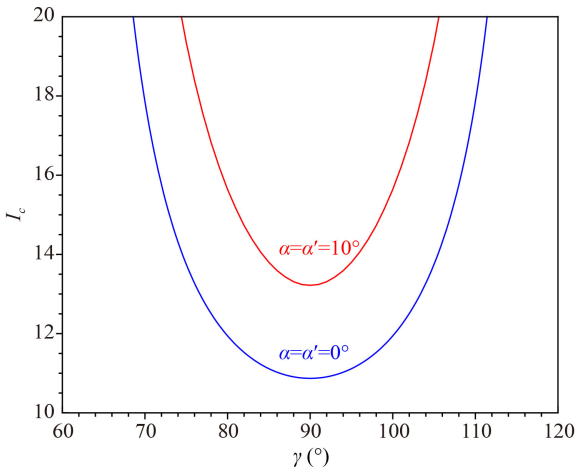

Fig. 3 The evolution as a function of triaxiality γ of the separatrix between dynamical phases with one and two minima represented by the critical angular momentum I_c for $j = j' = 11/2$ with and without tilting.

$$\begin{aligned}\mathcal{I}_1 &= \sqrt{I^2 - x^2}\cos\varphi,\\ \mathcal{I}_2 &= \sqrt{I^2 - x^2}\sin\varphi,\\ \mathcal{I}_3 &= x.\end{aligned} \tag{3.5}$$

Within this three-dimensional space, the constant classical energy is an ellipsoid displaced by the linear cranking terms:

$$\begin{aligned}\mathcal{H}(\mathcal{I}_1,\mathcal{I}_2,\mathcal{I}_3) =& \frac{I}{2}(A_1+A_2+A_3)\\ &+\frac{(2I-1)}{2I}(A_1\mathcal{I}_1^2+A_2\mathcal{I}_2^2+A_3\mathcal{I}_3^2)\\ &-2A_1\mathcal{I}_1 j\cos\alpha - 2A_2\mathcal{I}_2 j'\cos\alpha'\\ &-2A_3\mathcal{I}_3(j\sin\alpha + j'\sin\alpha').\end{aligned} \tag{3.6}$$

The other constant of motion, that is the total angular momentum squared, is represented by a sphere $\sum\mathcal{I}_k^2 = I^2$. The intersection of these two surfaces defines the classical trajectory of the total angular momentum vector. Note that the sum of classical averages for the squared operators would result in $\sum\langle\hat{I}_k^2\rangle = I(I+1)$, which reflects the fact that the variational state is an eigenfunction for the $\hat{I}^2$ operator [46]. Examples of such classical trajectories are given in Fig. 4, corresponding to the same triaxiality and alignment conditions used in Fig. 1. The variation of the classical energy function depicted in Fig. 1 becomes now more clear given the similarity between its constant energy contours and the intersection curves of Fig. 4. When $\gamma = 90°$, the radially displaced ellipsoid of the classical energy is symmetrical and aligned with its symmetry axis along the third principal axis. For $\gamma > 90°$, the ellipsoid keeps its position but generate a skewed intersection curve due to its deformation. On the other hand, the tilting shifts the classical energy ellipsoid higher along the third principal axis.

4 Quantum observables

Although the classical description provides the time dependent evolution of the system's rotation, it cannot be extended for the purely quantum concept of superposition between the chiral solutions with opposite handedness. This can be achieved only in a quantum setting. One can however maintain the information from the classical picture by quantizing the classical energy function through the correspondence principle applied to the canonical conjugate coordinates, whose time evolution is well understood. The quantization procedure is not trivial, more so because the classical energy function has mixed terms of generalized coordinate and momentum and involves square roots and trigonometric functions of them, which must be expanded prior to quantization. The classical energy function in the presently working triaxiality and alignment configuration, has always a single minimum along the azimuth angle coordinate φ. This property is used to approximate the classical energy function to be quantized, by its harmonic expansion around the corresponding minimum points in $\varphi_0(x)$ for fixed values of x:

$$\tilde{\mathcal{H}}(x,\varphi) \approx \mathcal{H}(x,\varphi_0(x)) + \frac{1}{2}\left(\frac{\partial^2\mathcal{H}}{\partial\varphi^2}\right)_{\varphi_0(x)}[\varphi-\varphi_0(x)]^2. \tag{4.1}$$

The minimum points $\varphi_0(x)$ are the values which minimize the energy function for a fixed chiral variable x. The function $\varphi_0(x)$ is obtained from the condition $\partial\mathcal{H}(x,\varphi)/\partial\varphi = 0$ which leads to a quartic equation for $\cos\varphi_0(x)$:

$$\begin{aligned}&(2I-1)\sqrt{I^2-x^2}(A_2-A_1)\cos\varphi_0(x)\sin\varphi_0(x)\\ &\quad= 2I\left[A_2 j'\cos\varphi_0(x)\cos\alpha' - A_1 j\sin\varphi_0(x)\cos\alpha\right].\end{aligned} \tag{4.2}$$

As can be seen from Fig. 1, $\varphi_0 = const.$ when $\gamma = 90°$, otherwise the above equation has a single physical solution [39]. After a symmetrization of coordinate and momentum mixed terms, the approximated classical energy function is quantized by the correspondence $\varphi = \mathrm{i}\frac{\mathrm{d}}{\mathrm{d}x}$ in the momentum space. This leads to the following Schrödinger equation

$$\left[-\frac{1}{2}\frac{1}{\sqrt{B(x)}}\frac{\mathrm{d}}{\mathrm{d}x}\frac{1}{\sqrt{B(x)}}\frac{\mathrm{d}}{\mathrm{d}x} + V(x)\right]f(x) = Ef(x), \tag{4.3}$$

which is written in a particular form of a more general kinetic term involving coordinate-dependent effective mass [47]:

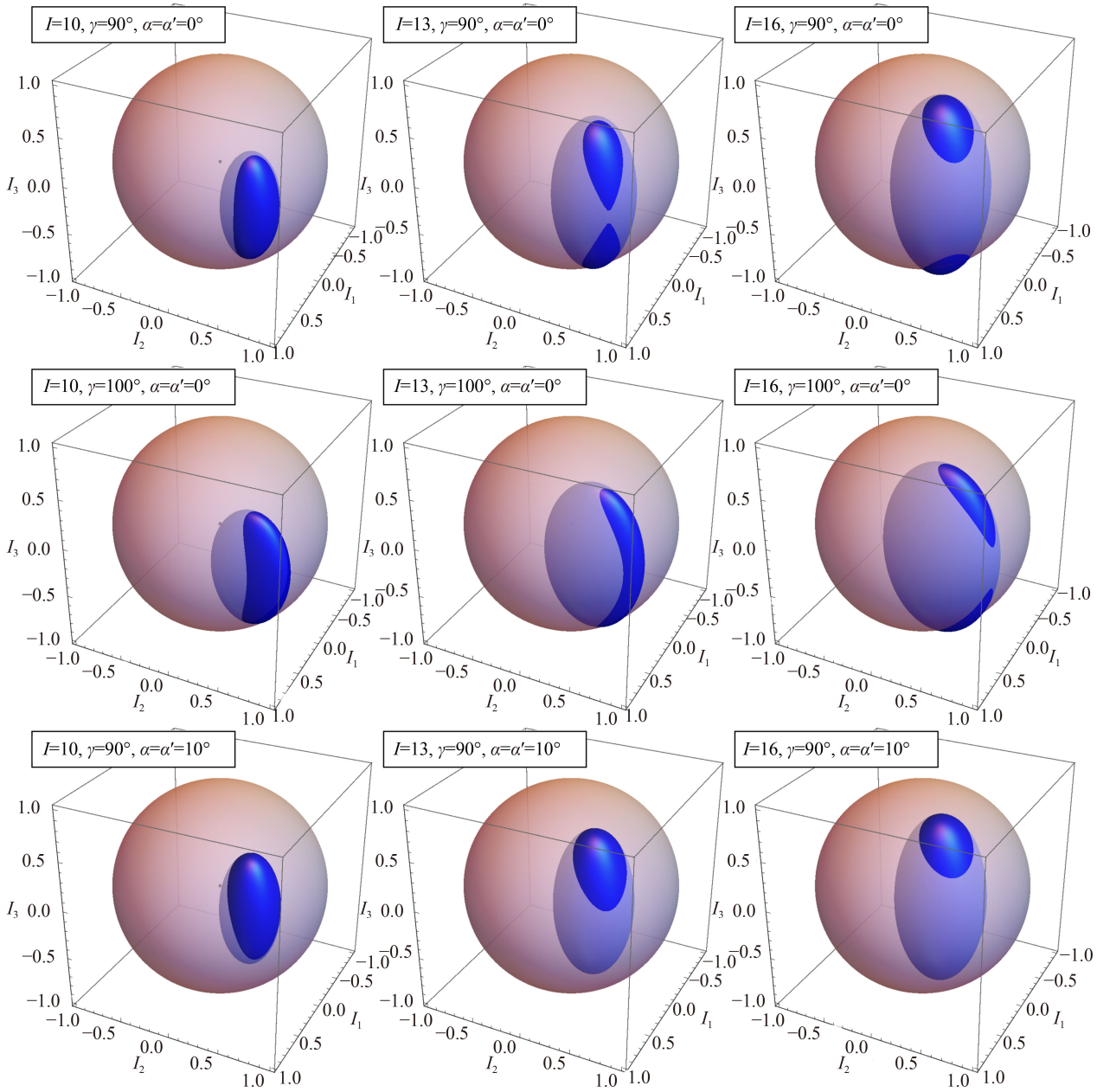

Fig. 4 Classical trajectories given as intersection of the surfaces corresponding to constants of motion in the space of classical angular momentum projections $\{\mathcal{I}_1, \mathcal{I}_2, \mathcal{I}_3\}$ in units of I. Trajectories are presented for $I = 10, 13, 16$ in absence of tilting when $\gamma = 90°$ (first row) and $\gamma = 100°$ (second row), as well as for a $\alpha = \alpha' = 10°$ tilting when $\gamma = 90°$ (last row). The classical energy value is taken as the ground state eigenvalue for the corresponding spin taken form Refs. [38–40].

$$B(x) = \left[\frac{\partial^2 \mathcal{H}(x,\varphi)}{\partial \varphi^2}\right]^{-1}_{\varphi_0(x)} = \left\{\frac{2I-1}{I}(I^2-x^2)(A_2-A_1)\cos 2\varphi_0(x) + 2\sqrt{I^2-x^2} \times \left[A_1 j \cos\varphi_0(x)\cos\alpha + A_2 j' \sin\varphi_0(x)\cos\alpha'\right]\right\}^{-1}. \tag{4.4}$$

The potential for the chiral variable in the above equation is defined as

$$V(x) = \mathcal{H}(x,\varphi_0(x)) + \frac{B''(x)}{8\left[B(x)\right]^2} - \frac{9\left[B'(x)\right]^2}{32\left[B(x)\right]^3}. \tag{4.5}$$

The coordinate-dependent effective mass redefines the scalar product such that the normalization condition for function $f(x)$ reads

$$\int |f(x)|^2 \sqrt{B(x)}\mathrm{d}x = 1. \tag{4.6}$$

At this point, one can see that the harmonic approximation, performed before the quantization procedure, is

meant to truncate the quantum expansion up to $\frac{d^2}{dx^2}$. In this way, the complicated classical energy function is cast into a second order Schrödinger equation with separated kinetic and potential terms. The later keeps the entire classical behaviour of the chiral variable which is quantized without any approximation. As a matter of fact, one can see from Figs. 5 and 6 that the chiral potential follows very closely the minimum valley profile of the corresponding classical energy function. It is worth to mention here that similar quantum Hamiltonians were semiclassically constructed based on the tilted axis cranking for the description of both chiral [35–37] and wobbling modes [48, 49].

The evolution with spin of the quantum model in terms of effective mass and the chiral potential with its corresponding ground and excited states is shown in Figs. 5 and 6. The chiral potential changes from a single well shape at small angular momentum values to a double well structure at a faster rotation. Without tilting, the potential is symmetric in respect to $x = 0$ and its two minima are degenerated, while in the presence of tilting the $\pm x$ symmetry is broken, shifting thus the single minimum to $x > 0$ position and inducing an energy split for the two chiral minima. The effective mass has a general structure with a relatively shallow minimum at $x = 0$, which becomes flatter with spin. The tilting has a negligible effect on the effective mass, while the departure from maximal triaxiality makes the small spin minimum sharper and at the same time flattens more the high spin effective masses.

The quantum states are obtained within a diagonalization procedure using a basis of particle in the box wave-functions:

$$\begin{aligned} f_I^s(x) =& F_I^s(x)\,[B(x)]^{-\frac{1}{4}} \\ =& \frac{[B(x)]^{-\frac{1}{4}}}{\sqrt{I}} \left\{ \sum_{n=1}^{n_{\max}} A_n^s \cos\left[\frac{(2n-1)\pi x}{2I}\right] \right. \\ &\left. + \sum_{n=1}^{n_{\max}} B_n^s \sin\left(\frac{2n\pi x}{2I}\right) \right\}, \end{aligned} \tag{4.7}$$

which is a suitable choice given the fact that the chiral variable is already physically bounded by $|x| < I$. The diagonalization solutions are indexed by the order s serving as a chiral quantum number. The convergence of the diagonalization results is achieved around the truncation dimension $n_{\max} = 100$. The wave function determined from the diagonalization procedure is used to define the density probability for the active chiral variable

$$\rho_I^s(x) = |F_I^s(x)|^2 = |f_I^s(x)|^2 \sqrt{B(x)}, \tag{4.8}$$

from which one can ascertain the system's quantum dynamics. For example, from Figs. 5 and 6, one can see that the initial stage is always represented by single peak probability distribution for the ground state and a

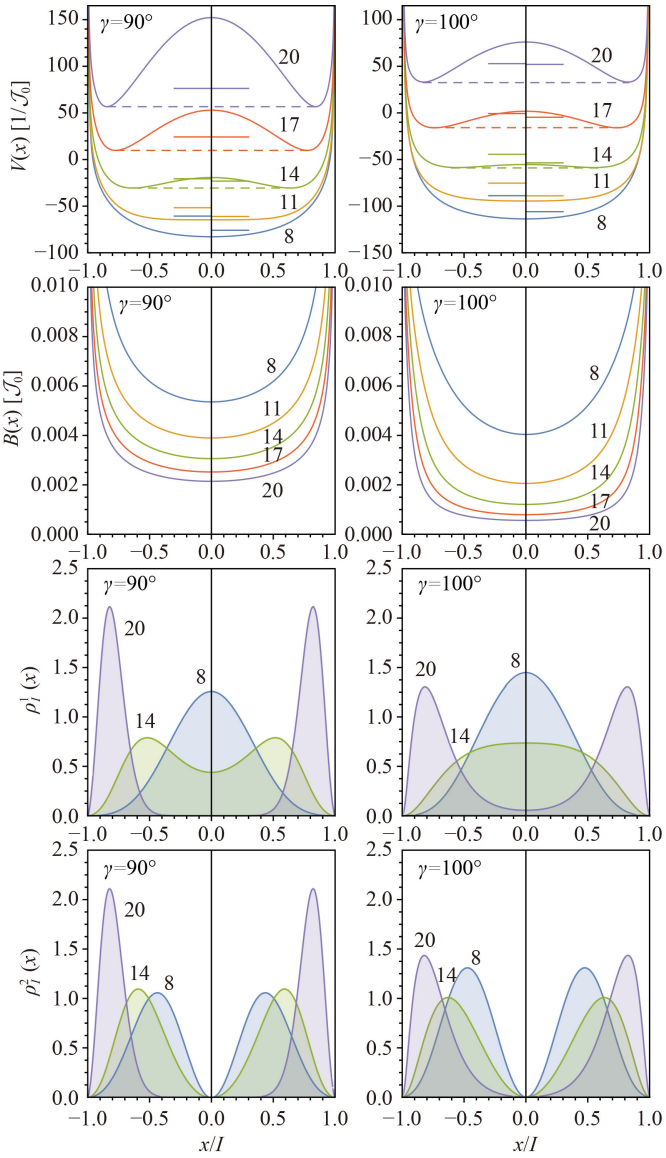

Fig. 5 The chiral potential (first row), effective mass (second row), yrast state $s = 1$ (third row) and excited state $s = 2$ (fourth row) probability distribution defined by Eq. (4.8), are represented as a function of the normalized chiral variable x/I for a selection of I values, in the absence of titling ($\alpha = \alpha' = 0$) when $\gamma = 90°$ and $\gamma = 100°$. The single-particle spins are $j = j' = 11/2$.

double peak for the excited state. The later denote the vibrational character of the excitation [30]. After the critical angular momentum, the system's dynamics changes in particular ways for specific titling conditions. In the absence of tilting, the ground state probability distribution shown in Fig. 5 starts to split into two identical peaks, reaching at high angular momentum the same shape as for the excited state. Basically, the quantum system undergoes a gradual change from an anharmonic chiral vibration to static chirality, through intermediate instances of double well vibration with and without

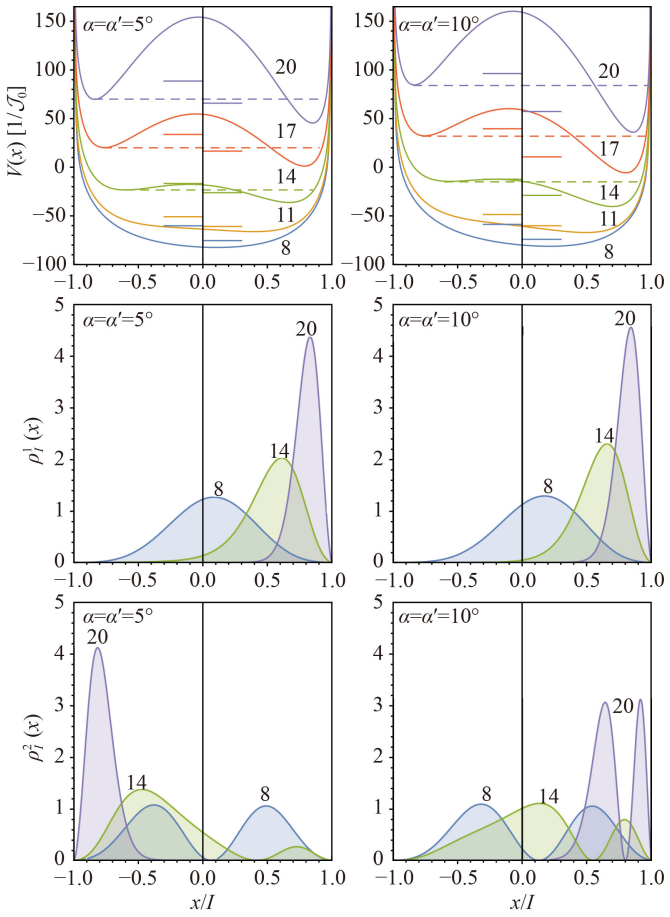

Fig. 6 The chiral potential (first row), yrast state $s = 1$ (second row) and excited state $s = 2$ (third row) probability distribution defined by Eq. (4.8), are represented as a function of the normalized chiral variable x/I for a selection of I values, when $\gamma = 90°$ with $\alpha = \alpha' = 5°$ and $\alpha = \alpha' = 10°$ tilting. The single-particle spins are $j = j' = 11/2$.

tunneling. Given the equivalence of the two chiral configurations in the absence of tilting, the ground and excited states in the static chirality established at high spins are defined as symmetric and antisymmetric superpositions of right and left handed intrinsic chiral solutions. This dynamical evolution is valid for a wide range of triaxiality. Note however that when the system has a smaller triaxiality $\gamma \lesseqgtr 90°$, the discussed transition commences at a later value of angular momentum and retains a non-vanishing planar $(x = 0)$ contribution in both ground and excited states [50].

When there is a tilting, the chiral symmetry is broken and the two potential minima which appear after the critical point are no longer equivalent. Even a small tilting has dramatic consequences on the symmetry of the system, despite a negligible energy difference between the two configurations. In this situation the ground and excited state gradually acquire a well defined handedness, by favoring through their probability distributions the lowest and respectively the second potential energy minimum. The process depicted in Fig. 6 involves a highly anharmonic stage with tunneling effects which transfers the probability from the favored vibrational turning point to the unfavored one in the excited state, while the ground state just moves its centroid in the tilting direction.

As can be seen in Fig. 6, a quite different high spin dynamical regime takes place at an increased tilting. Indeed, for a larger energy split between the two chiral configurations, the vibrational excitation within the lowest minimum becomes energetically favorable to a static configuration with opposite chirality. Although the ground state behaves similarly to the small tilting case, the excited state retains its double peak vibrational nature for all angular momentum states. At high spin, both turning points of the vibrational excitation become confined to the favored chiral configuration, that is within the lowest potential minimum. From the phenomenological point of view, one can say that the system undergoes a transition from an asymmetric chiral vibration to an aplanar wobbling motion around the favored chiral configuration.

The spectral consequences of the different dynamical regimes described above are shown in Fig. 7. In the absence of tilting, the energy splitting $\Delta E(I) = E_{I2} - E_{I1}$ between ground and excited states decreases with spin to the zero value which marks the establishment of static chirality, where the symmetric and antisymmetric superpositions of chiral solutions are degenerated. The decreasing trend of the energy difference between ground and excited states is maintained for a shorter interval with increasing tilting. Moreover, the static asymmetric chirality is identified by a non-zero minimum in the energy difference, which further increases linearly with spin. The static chirality and respectively energy degeneracy or the minimum is reached later for smaller triaxiality. The high spin linear increase of energy difference have approximately the same slope for different triaxiality and the same tilting.

The obtained wave functions can be further employed to determine the coefficients

$$\Lambda_{IKs} = \left\{ \sum_{K=-I}^{I} [F_I^s(K)]^2 \right\}^{-1/2} F_I^s(K) \tag{4.9}$$

of the total wave function expansion in rotation matrices

$$|\Psi_{IMs}\rangle = \sum_{K=-I}^{I} \Lambda_{IKs} |IKM\rangle. \tag{4.10}$$

The $|\Lambda_{IKs}|^2$ designate discrete points on the continuous density distribution (4.8). This expansion is then used to calculate various electromagnetic properties. Of special interest are the $E2$ and $M1$ electromagnetic transition probabilities. If one considers the more general $E2$ transition operator

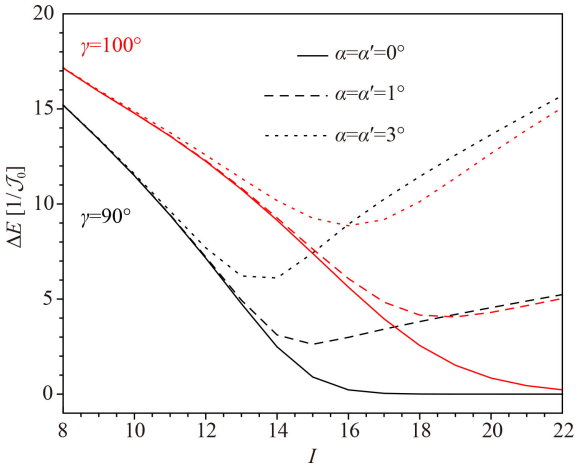

Fig. 7 Theoretical energy differences between the states of the partner bands ($s=1$ and $s=2$) as a function of angular momentum for different tilting $\alpha=\alpha'=0°, 1°, 3°$ of the quasiparticle spins when triaxiality is $\gamma=90°$ and $\gamma=100°$.

$$T_{2\mu}(E2) = t_1 q_{2\mu} + t_2 \left[q \times q\right]_{2\mu}, \tag{4.11}$$

up to a quadratic term in quadrupole moments $q_{2\mu}$, the corresponding transition probability acquires the following expression:

$$B(E2; Is \to I's') = \frac{5}{16\pi} \left| \sum_{K,K'} \Lambda^*_{IKs} \Lambda_{I'K's'} \times \left[\tilde{Q}_0 C^{I\,2\,I'}_{K\,0\,K'} + \frac{\tilde{Q}_2}{\sqrt{2}} \left(C^{I\,2\,I'}_{K\,2\,K'} + C^{I\,2\,I'}_{K\,-2\,K'} \right) \right] \right|^2 . \tag{4.12}$$

The redefined quadrupole components are given as

$$\tilde{Q}_0 = Q \left(\cos\gamma - \chi\beta \sqrt{\frac{2}{7}} \cos 2\gamma \right),$$
$$\tilde{Q}_2 = Q \left(\sin\gamma + \chi\beta \sqrt{\frac{2}{7}} \sin 2\gamma \right), \tag{4.13}$$

where Q is an empirical quadrupole moment value, β is the quadrupole deformation, while $\chi = t_2/t_1$ is an adjustable parameter of the relative contribution of the two terms from (4.11).

For the $M1$ transition operator, the relevant expression reduces to

$$T_{1\mu}(M1) = \sqrt{\frac{3}{4\pi}} \mu_N \sum_{\nu=0,\pm1} \left(g_{eff} j_\nu + g'_{eff} j'_\nu \right) D^1_{\mu\nu}, \tag{4.14}$$

where $g_{eff} = g_j - g_R$ and $g'_{eff} = g_{j'} - g_R$ are the effective gyromagnetic factors obtained from the corresponding values of the core and of the involved single-particle orbitals. In order to obtain the final formula for the corresponding transition probability, one considers the spherical components of the single-particle spin in accordance to the frozen alignment condition (2.4):

$$j_\pm = \mp \frac{j\cos\alpha}{\sqrt{2}}, \quad j'_\pm = -\frac{\mathrm{i} j' \cos\alpha'}{\sqrt{2}},$$
$$j_0 = j\sin\alpha, \quad j'_0 = j'\sin\alpha'. \tag{4.15}$$

In the end, the expression for the $M1$ transition probability reads:

$$B(M1; Is \to I's') = \frac{3}{4\pi}\mu_N^2 \left| \sum_{K,K'} \Lambda^*_{IKs} \Lambda_{I'K's'} \times \left[\frac{g_{eff} j \cos\alpha}{\sqrt{2}} \left(C^{I\,1\,I'}_{K\,1\,K'} - C^{I\,1\,I'}_{K\,-1\,K'} \right) + \frac{\mathrm{i} g'_{eff} j' \cos\alpha'}{\sqrt{2}} \left(C^{I\,1\,I'}_{K\,1\,K'} + C^{I\,1\,I'}_{K\,-1\,K'} \right) - \left(g_{eff} j \sin\alpha + g'_{eff} j' \sin\alpha' \right) C^{I\,1\,I'}_{K\,0\,K'} \right] \right|^2 .$$

5 Numerical applications

For a quantitative description of chiral partner bands, one considers the following formula for the total energy:

$$E_{Is} = E^{diag}_{Is}(\mathcal{J}_0, \gamma, \alpha, \alpha') + CI(I+1) + E_0. \tag{5.1}$$

The first term denotes the eigenvalue of order s determined from the diagonalization of Eq. (4.3), which is parametrized by the triaxiality γ, tilting angles α and α', and the scaling MOI $\mathcal{J}_0$. This energy is amended with a rotational contribution which does not affect the structure of total quantum system because the total wave function is an eigenfunction of the $\hat{J}^2$ operator. This rotational correction is meant to reproduce the experimental rotation spectrum without compromising the evolution with spin of the energy difference between the partner band states. In comparison, the PRM calculations sometimes employ for this purpose a spin dependent scaling MOI. Finally, the last term is a reference energy which accounts for the constant single-particle contribution omitted from (2.1). Having both triaxiality and tilting adjustable is not yet computationally tractable. Therefore, the triaxiality is a priori fixed to $\gamma = 90°$. The system's dynamics changes very little in close vicinity of this value, as can be attested by the shallow minimum of the separatrix between the two chiral modes shown in Fig. 3. Moreover, this restriction is consistent with the described phenomenon of chirality, which is directly correlated with high triaxiality of nuclei. With a fixed triaxiality, the model reduces to five adjustable parameters for energy levels: α, α', $\mathcal{J}_0$, C, and E_0. Despite the relatively large number of parameters, the aspects of chirality, as

Table 1 The quasiparticle spins with the alignment angles α and α' are listed together with parameters $\mathcal{J}_0$ (MeV^{-1}), E_0 (MeV), and C (keV) obtained by fitting the experimental excitation energies of ^{118}I [51], ^{134}Pr [9,52], and ^{138}Pm [53]. The fitting performance is ascertained by the *rms* values given in the last column.

Nucl.	j (hole)	j' (particle)	α	α'	E_0 (MeV)	$\mathcal{J}_0$ (MeV^{-1})	C (keV)	*rms* (keV)
^{119}I	$\frac{9}{2}$ (π)	$\frac{11}{2}$ (ν)	3°	10°	2.293	29.294	0.19	61.4
^{134}Pr	$\frac{11}{2}$ (ν)	$\frac{11}{2}$(π)	3°	3°	1.759	48.076	3.24	43.9
^{138}Pm	$\frac{11}{2}$ (ν)	$\frac{11}{2}$(π)	0°	8°	2.303	35.681	3.34	31.4

for example the energy difference $\Delta E(I) = E_{I2} - E_{I1}$, depends up to a scaling factor only on the tilting angles.

Although there are dozens of chiral bands reported in various regions of the nuclide chart [9], very few instances of experimental data fall into the generally accepted behavior for the chiral partner bands. From previous iterations of the model [38, 40] and after a brief survey of the updated experimental data, one obtained the best results for the proposed $\pi(g_{9/2})^{-1}\nu h_{11/2}$ chiral bands in ^{118}I [51], as well as for the traditional $\pi h_{11/2}\nu(h_{11/2})^{-1}$ chiral candidates in ^{134}Pr [9, 52] and ^{138}Pm [53]. The experimental partner bands for the ^{134}Pr nucleus are selected according to Ref. [52], where the second and third $\pi h_{11/2}\nu(h_{11/2})^{-1}$ bands are designated as partner bands, in contradiction to the earlier studies [3, 15–17, 54, 55]. The results from fitting the experimental energy levels of the considered nuclei with formula (5.1), are listed in Table 1. The resulted theoretical spectra are compared with their experimental counterparts in Fig. 8, where one also shown the same comparison for the energy difference between partner bands. The listed *rms* values compared with the average experimental rotational excitations, as well as the comparison made in Fig. 8 demonstrates a very good agreement with data for the selected nuclei. It is worthy to mention that the theory reproduces accurately the attraction and then the repulsion of the two bands, as well as the position of the minimum of the energy difference between bands.

The fitted parameters suggest a sizable tilting of both proton hole and neutron particle spins in ^{118}I, with a higher deviation for the neutron. For the $\pi h_{11/2}\nu(h_{11/2})^{-1}$ chiral bands, the model calculation are invariant to the change between α and α', because $j = j'$ and $A_1 = A_2$ when $\gamma = 90°$. This is not important for the ^{134}Pr nucleus, where the fits produce the same small tilting for both proton and neutron spins. However, for the ^{138}Pm one obtains an asymmetrical tilting with one of the single particle spins fully aligned to its corresponding principal axis. The findings of Ref. [56] solve this problem by showing that only the dominant proton quasiparticle configuration has a sizable medium axis component. It is worth to mention that the results for the ^{134}Pr nucleus, are consistent with its general accepted title of the best example of chiral geometry. Indeed, the relatively small tilting of the whole plane of the two quasiparticle spins, imply a near degeneracy of the chiral partner bands at least locally. As a matter of fact, despite slightly lower $1/\mathcal{J}_0$ scale, the absolute values of the energy difference for this nucleus are very small in comparison for example with the case of ^{138}Pm, reaching a minimum of only 120 keV at $I = 13 - 14$. Analysis on the diagonalization wave-functions, showed that all three nuclei undergo a transition from an asymmetric chiral vibration to a regime where the yrast and excited states acquire opposite chirality. The chiral vibration is found to cease at $I = 13$ in ^{118}I nucleus, and at $I = 14$ for the other two nuclei.

One must mention that the fitting procedure produced a very shallow minimum in the parameter space of α and α', that is fits with similar $\alpha + \alpha'$ provided very close *rms* values [40]. Nevertheless, these $\alpha + \alpha'$ minima are also consistent with those obtained when fitting only the energy difference between the two bands, which up to a scale depend only on these two angles and the triaxiality which is already fixed (see Fig. 7). This aspect adds confidence for the model results regarding the overall tilting of the quasiparticle plane, but individual quasiparticle alignments must be corroborated with microscopic studies as was done above for ^{138}Pm or with their distinct effect on the rotational sequence of the two bands.

The description of the chiral bands in ^{134}Pr and ^{138}Pm is completed by calculations on their electromagnetic properties which have corresponding measured data. Thus, one considers a 0.6 quenching of the free nucleon spin gyromagnetic factors and a rotor estimation $g_R = Z_c/A_c$ of the core gyromagnetic factor in $M1$ transitions. For a better reproduction of data, the empirical quadrupole moment Q and the parameter χ involved in the electric transition probability are fitted to available experimental data with the inclusion of errors. As a result, one obtained $Q = 8\,eb$ and $\chi = -5.39$ for ^{134}Pr, respectively $Q = 11.21\,eb$ and $\chi = -3.38$ for ^{138}Pm. The $E2$ transition probability also depends on quadrupole deformation. The values $\beta = 0.207$ for ^{134}Pr and $\beta = 0.17$ for ^{138}Pm were collected from Ref. [57]. The comparison with available experimental data regarding often used $B(M1; I \to I-1)/B(E2; I \to I-2)$ ratios, is presented in Fig. 9. Both theoretical and experimental values have a general decreasing trend with spin. Theoretical calculations predict a large difference between bands at low spins, with higher values reported for the first band. Then the

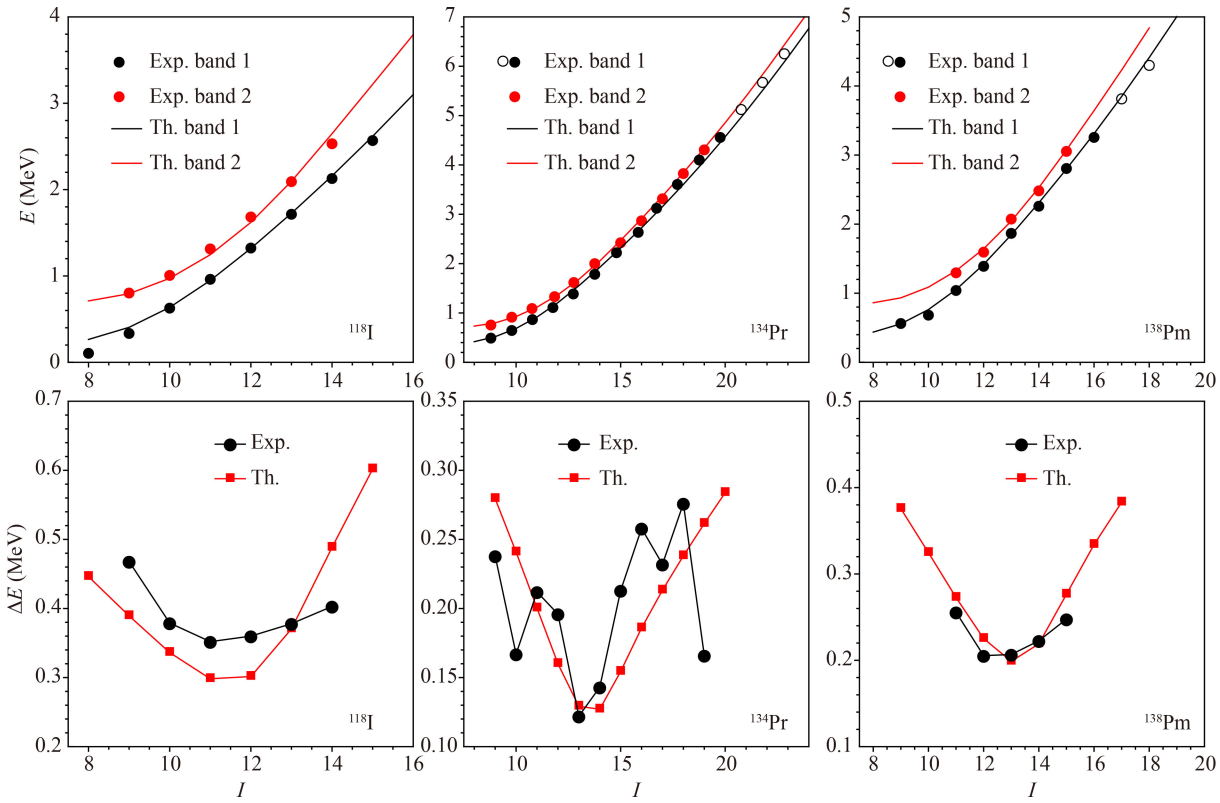

Fig. 8 Comparison between experimental and theoretical energies of the partner bands (top), and the corresponding energy differences (bottom) for ^{118}I [51], ^{134}Pr [9,52] and ^{138}Pm [53] as functions of total angular momentum. Only data points with filled symbols where included in the fitting procedure.

two bands acquire similar theoretical values at $I = 15$ in both nuclei. These aspects are more or less confirmed by the experimental data. Indeed the low spin experimental $B(M1)/B(E2)$ ratios are very distinct at small spins, merging exactly at $I = 15$ for the ^{138}Pm nucleus, and later at $I = 16$ in ^{134}Pr. As a matter of fact, in the later case, $I = 16$ marks the inversion of the experimental values corresponding to the two bands, with the band 2 having now the higher value, but not by much as in the case of the low spin interval. The theoretical results for the ^{134}Pr nucleus reproduce this trend. Note that the difference between the bands diminishes with increasing spin. A similar interval of higher $B(M1)/B(E2)$ values for the second band is also theoretically predicted for the ^{138}Pm nucleus, which is however short lived. It is worth to mention that the relative spin dependence of the two bands is exclusively dictated by the tilting geometry, the additional parameter χ fixes just the general behaviour of the $B(M1)/B(E2)$ ratio within the two bands as a function of angular momentum.

6 Conclusions

The dynamics associated with the chiral symmetry in nuclei was described in a semiclassical manner. The semiclassical method is extensively presented. Thus, the classical energy and the equations of motions for a chiral system composed of a triaxial core with rigidly aligned single-particle spins were extracted from a quantum rotor Hamiltonian cranked by quasiparticle alignments, by means of a time-dependent variational principle with an angular momentum coherent state as a variational function. The later is parametrized by the azimuth angle and a chiral projection variable associated with the direction of the total angular momentum vector. This parametrization cast the equations of motion into a Hamilton canonical form, establishing a canonical conjugate relationship between the two directional variables of the total angular momentum vector. The evolution with angular momentum of the classical energy function for various deformation and alignment conditions was presented by tracking the coordinates of the stationary points. As a result of this analysis, were identified distinct dynamical modes with specific existence conditions. Alternatively, the classical trajectories surrounding the stationary points were schematically visualized in the space of classical components of total angular momentum. The ability of the model to account for the quantum aspects of the chirality is demonstrated by constructing a quantum Hamiltonian for the chiral variable which achieves a natural separation of kinetic and

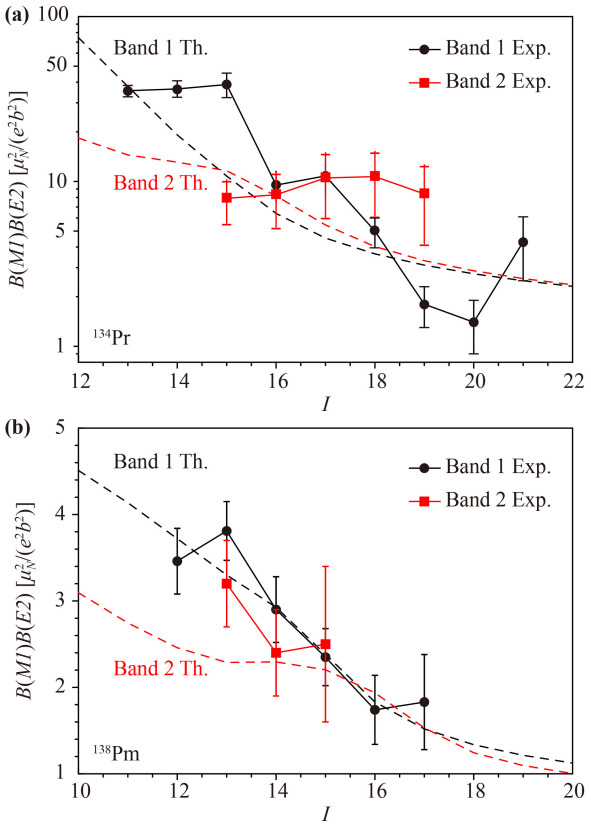

Fig. 9 Comparison between experimental and theoretical $B(M1)/B(E2)$ values for bands 1 and 2 of ^{134}Pr **(a)** [52] and ^{138}Pm **(b)** [53].

potential energies. Consequently, the relevant quantum observables deduced from the reconstructed quantum picture retain most of the dynamical aspects discerned in the classical analysis. Numerical applications regrading quantum observables predict specific spectral signatures related to chirality in general and particularly to the transition between its distinct modes: chiral vibration, static chirality, three-dimensional wobbling. These aspects are confirmed by few experimental realizations of the model in what concerns energy levels and electromagnetic transitions.

Before closing, it is instructive to discuss possible prospects regarding this approach. It is an excellent tool to describe dynamical effects, but as was mentioned before, for quantitative results, effective fits with variable triaxiality and tilting are computationally demanding. However, one can always employ a triaxiality measure from other sources and perform similar calculations as presented here. On the other hand, the cranked Hamiltonian (2.5) can be exactly diagonalized for any values of γ, α and α'. The results can be used as a first step in determining the optimal deformation and alignment geometry for a certain nucleus. Fine fits around this parameter set can then be used to fix the parameters of Eq. (5.1). One expects a small difference between exact diagonalization results and those coming from the Schrödinger equation. However, the latter has a separated potential in a continuous variable related to the projection of the total angular momentum, carrying important dynamical information which cannot transpire from the discrete space of angular momentum operators. Another venue of development is related to the exploitation of the frozen alignment approximation. Although it is considered as the major drawback, it can be used to study the Coriolis interaction and the rotational alignment of the involved quasiparticles. Indeed, fixing the model parameters to few low lying states, one can extend the model by adjusting only the tilting angles to reproduce the higher excited states, providing thus information about the dynamical evolution in quasiparticle alignments.

In conclusion, the semiclassical approach is a viable alternative for the description of nuclear chirality. It's essential distinction from the PRM resides in the fact that the chiral geometry is a starting hypothesis. Although for tractable calculations one must allow some approximations, the resulted model analysis serves as a useful reference for the origin and various aspects of the chiral symmetry breaking. The advantage of the classical and quantum duality is reflected in the classical description of the rotational dynamics in terms of relevant degrees of freedom, which are further used to quantize the fluctuations around or between identified stable rotational configurations. As a final remark one must mention that the presented semiclassical formalism is easily transposable to the description of wobbling excitations [58–61].

Acknowledgements This work was supported by a grant of the Ministry of Research, Innovation and Digitalization, CNCS - UEFISCDI, project number PN-III-P1-1.1-TE-2021-0109, within PNCDI III.

References

1. S. Frauendorf and J. Meng, Tilted rotation of triaxial nuclei, *Nucl. Phys. A* 617(2), 131 (1997)
2. S. Frauendorf, Spontaneous symmetry breaking in rotating nuclei, *Rev. Mod. Phys.* 73(2), 463 (2001)
3. K. Starosta, T. Koike, C. J. Chiara, D. B. Fossan, D. R. LaFosse, A. A. Hecht, C. W. Beausang, M. A. Caprio, J. R. Cooper, R. Krücken, J. R. Novak, N. V. Zamfir, K. E. Zyromski, D. J. Hartley, D. L. Balabanski, J. Zhang, S. Frauendorf, and V. I. Dimitrov, Chiral doublet structures in odd–odd $N = 75$ isotones: Chiral vibrations, *Phys. Rev. Lett.* 86(6), 971 (2001)
4. J. Meng and S. Q. Zhang, Open problems in understanding the nuclear chirality, *J. Phys. G* 37(6), 064025 (2010)
5. J. Meng, Q. B. Chen, and S. Q. Zhang, Chirality in atomic nuclei: 2013, *Int. J. Mod. Phys. E* 23(11), 1430016 (2014)
6. R. A. Bark, E. O. Lieder, R. M. Lieder, E. A. Lawrie, J. J. Lawrie, S. P. Bvumbi, N. Y. Kheswa, S. S. Ntshangase, T. E. Madiba, P. L. Masiteng, S. M.

Mullins, S. Murray, P. Papka, O. Shirinda, Q. B. Chen, S. Q. Zhang, Z. H. Zhang, P. W. Zhao, C. Xu, J. Meng, D. G. Roux, Z. P. Li, J. Peng, B. Qi, S. Y. Wang, and Z. G. Xiao, Studies of chirality in the mass 80, 100 and 190 regions, *Int. J. Mod. Phys. E* 23(7), 1461001 (2014)
7. A. A. Raduta, Specific features and symmetries for magnetic and chiral bands in nuclei, *Prog. Part. Nucl. Phys.* 90, 241 (2016)
8. K. Starosta and T. Koike, Nuclear chirality, a model and the data, *Phys. Scr.* 92(9), 093002 (2017)
9. B. W. Xiong and Y. Y. Wang, Nuclear chiral doublet bands data tables, *At. Data Nucl. Data Tables* 125, 193 (2019)
10. S. Y. Wang, Recent progress in multiple chiral doublet bands, *Chin. Phys. C* 44(11), 112001 (2020)
11. J. Meng, J. Peng, S. Q. Zhang, and S. G. Zhou, Possible existence of multiple chiral doublets in ^{106}Rh, *Phys. Rev. C* 73(3), 037303 (2006)
12. B. F. Lv, C. M. Petrache, A. Astier, E. Dupont, A. Lopez-Martens, P. T. Greenlees, H. Badran, T. Calverley, D. M. Cox, T. Grahn, J. Hilton, R. Julin, S. Juutinen, J. Konki, M. Leino, J. Pakarinen, P. Papadakis, J. Partanen, P. Rahkila, M. Sandzelius, J. Saren, C. Scholey, J. Sorri, S. Stolze, J. Uusitalo, A. Herzán, B. Cederwall, A. Ertoprak, H. Liu, S. Guo, M. L. Liu, Y. H. Qiang, J. G. Wang, X. H. Zhou, I. Kuti, J. Timár, A. Tucholski, J. Srebrny, and C. Andreoiu, Evolution from γ-soft to stable triaxiality in ^{136}Nd as a prerequisite of chirality, *Phys. Rev. C* 98(4), 044304 (2018)
13. S. Guo, C. M. Petrache, D. Mengoni, Y. H. Qiang, Y. P. Wang, Y. Y. Wang, J. Meng, Y. K. Wang, S. Q. Zhang, P. W. Zhao, A. Astier, J. G. Wang, H. L. Fan, E. Dupont, B. F. Lv, D. Bazzacco, A. Boso, A. Goasduff, F. Recchia, D. Testov, F. Galtarossa, G. Jaworski, D. R. Napoli, S. Riccetto, M. Siciliano, J. J. Valiente-Dobon, M. L. Liu, G. S. Li, X. H. Zhou, Y. H. Zhang, C. Andreoiu, F. H. Garcia, K. Ortner, K. Whitmore, A. Ataç-Nyberg, T. Bäck, B. Cederwall, E. A. Lawrie, I. Kuti, D. Sohler, T. Marchlewski, J. Srebrny, and A. Tucholski, Evidence for pseudospin-chiral quartet bands in the presence of octupole correlations, *Phys. Lett. B* 807, 135572 (2020)
14. Y. Zhang, B. Qi, and S. Q. Zhang, Critical point symmetry for odd–odd nuclei and collective multiple chiral doublet bands, *Sci. China Phys. Mech. Astron.* 64(12), 122011 (2021)
15. S. Brant, D. Vretenar, and A. Ventura, Interacting boson fermion-fermion model calculation of the $\pi h_{11/2}\otimes\nu h_{11/2}$ doublet bands in ^{134}Pr, *Phys. Rev. C* 69(1), 017304 (2004)
16. D. Tonev, G. de Angelis, P. Petkov, A. Dewald, S. Brant, S. Frauendorf, D. L. Balabanski, P. Pejovic, D. Bazzacco, P. Bednarczyk, F. Camera, A. Fitzler, A. Gadea, S. Lenzi, S. Lunardi, N. Marginean, O. Möller, D. R. Napoli, A. Paleni, C. M. Petrache, G. Prete, K. O. Zell, Y. H. Zhang, J. Zhang, Q. Zhong, and D. Curien, Transition probabilities in ^{134}Pr: A test for chirality in nuclear systems, *Phys. Rev. Lett.* 96(5), 052501 (2006)
17. D. Tonev, G. Angelis, S. Brant, S. Frauendorf, P. Petkov, A. Dewald, F. Dönau, D. L. Balabanski, Q. Zhong, P. Pejovic, D. Bazzacco, P. Bednarczyk, F. Camera, D. Curien, F. D. Vedova, A. Fitzler, A. Gadea, G. L. Bianco, S. Lenzi, S. Lunardi, N. Marginean, O. Möller, D. R. Napoli, R. Orlandi, E. Sahin, A. Saltarelli, J. V. Dobon, K. O. Zell, J. Zhang, and Y. H. Zhang, Question of dynamic chirality in nuclei: The case of ^{134}Pr, *Phys. Rev. C* 76(4), 044313 (2007)
18. H. G. Ganev, A. I. Georgieva, S. Brant, and A. Ventura, New description of the doublet bands in doubly odd nuclei, *Phys. Rev. C* 79(4), 044322 (2009)
19. B. Qi, S. Q. Zhang, J. Meng, S. Y. Wang, and S. Frauendorf, Chirality in odd-A nucleus ^{135}Nd in particle rotor model, *Phys. Lett. B* 675(2), 175 (2009)
20. I. Hamamoto, Possible presence and properties of multi-chiral-pair bands in odd–odd nuclei with the same intrinsic configuration, *Phys. Rev. C* 88(2), 024327 (2013)
21. A. A. Raduta, C. M. Raduta, and A. Faessler, A new picture for the chiral symmetry properties within a particle–core framework, *J. Phys. G* 41(3), 035105 (2014)
22. Y. Y. Wang, S. Q. Zhang, P. W. Zhao, and J. Meng, Multiple chiral doublet bands with octupole correlations in reflection-asymmetric triaxial particle rotor model, *Phys. Lett. B* 792, 454 (2019)
23. A. Bohr and B. R. Mottelson, Nuclear Structure, Vol. 2, Benjamin, Reading, Massachusetts, 1975
24. G. H. Bhat, J. A. Sheikh, and R. Palit, Triaxial projected shell model study of chiral rotation in odd–odd nuclei, *Phys. Lett. B* 707(2), 250 (2012)
25. G. H. Bhat, R. N. Ali, J. A. Sheikh, and R. Palit, Investigation of doublet-bands in $^{124,\ 126,\ 130,\ 132}$Cs odd–odd nuclei using triaxial projected shell model approach, *Nucl. Phys. A* 922, 150 (2014)
26. F. Q. Chen, Q. B. Chen, Y. A. Luo, J. Meng, and S. Q. Zhang, Chiral geometry in symmetry-restored states: Chiral doublet bands in ^{128}Cs, *Phys. Rev. C* 96(5), 051303 (2017)
27. F. Q. Chen, J. Meng, and S. Q. Zhang, Chiral geometry and rotational structure for ^{130}Cs in the projected shell model, *Phys. Lett. B* 785, 211 (2018)
28. M. Shimada, Y. Fujioka, S. Tagami, and Y. R. Shimizu, Rotational motion of triaxially deformed nuclei studied by the microscopic angular-momentum-projection method. II. Chiral doublet band, *Phys. Rev. C* 97(2), 024319 (2018)
29. Y. K. Wang, F. Q. Chen, P. W. Zhao, S. Q. Zhang, and J. Meng, Multichiral facets in symmetry restored states: Five chiral doublet candidates in the even–even nucleus ^{136}Nd, *Phys. Rev. C* 99(5), 054303 (2019)
30. S. Mukhopadhyay, D. Almehed, U. Garg, S. Frauendorf, T. Li, P. V. M. Rao, X. Wang, S. S. Ghugre, M. P. Carpenter, S. Gros, A. Hecht, R. V. F. Janssens, F. G. Kondev, T. Lauritsen, D. Seweryniak, and S. Zhu, From chiral vibration to static chirality in ^{135}Nd, *Phys. Rev. Lett.* 99(17), 172501 (2007)
31. D. Almehed, F. Dönau, and S. Frauendorf, Chiral vibrations in the $A = 135$ region, *Phys. Rev. C* 83(5), 054308 (2011)
32. J. Meng and P. Zhao, Nuclear chiral and magnetic rotation in covariant density functional theory, *Phys. Scr.* 91(5), 053008 (2016)
33. P. W. Zhao, Multiple chirality in nuclear rotation: A

microscopic view, *Phys. Lett. B* 773, 1 (2017)
34. Z. X. Ren, P. W. Zhao, and J. Meng, Dynamics of rotation in chiral nuclei, *Phys. Rev. C* 105(1), L011301 (2022)
35. Q. B. Chen, S. Q. Zhang, P. W. Zhao, R. V. Jolos, and J. Meng, Collective Hamiltonian for chiral modes, *Phys. Rev. C* 87(2), 024314 (2013)
36. Q. B. Chen, S. Q. Zhang, P. W. Zhao, R. V. Jolos, and J. Meng, Two-dimensional collective Hamiltonian for chiral and wobbling modes, *Phys. Rev. C* 94(4), 044301 (2016)
37. X. H. Wu, Q. B. Chen, P. W. Zhao, S. Q. Zhang, and J. Meng, Two-dimensional collective Hamiltonian for chiral and wobbling modes. II. Electromagnetic transitions, *Phys. Rev. C* 98(6), 064302 (2018)
38. R. Budaca, Semiclassical description of chiral geometry in triaxial nuclei, *Phys. Rev. C* 98(1), 014303 (2018)
39. R. Budaca, Role of triaxiality in the structure of chiral partner bands, *Phys. Lett. B* 797, 134853 (2019)
40. R. Budaca, From chiral vibration to tilted-axis wobbling within broken chiral symmetry, *Phys. Lett. B* 817, 136308 (2021)
41. C. M. Raduta, A. A. Raduta, R. Poenaru, and Al. H. Raduta, Simultaneous description of wobbling and chiral properties in even–odd triaxial nuclei, *J. Phys. G* 49, 025105 (2022)
42. J. Frauendiener, Quadratic hamiltonians on the unit sphere, *Mech. Res. Commun.* 22(4), 313 (1995)
43. V. Lanchares, M. Inarrea, J. P. Salas, J. D. Sierra, and A. Elipe, Surfaces of bifurcation in a triparametric quadratic Hamiltonian, *Phys. Rev. E* 52(5), 5540 (1995)
44. S. Iida and M. Yamamura, Utility of the elliptic function for classical $SU(2)$-models of nuclear collective motions, *Prog. Theor. Phys.* 70(3), 783 (1983)
45. A. Gheorghe, A. A. Raduta, and V. Ceausescu, Semiclassical treatment of the cranked triaxial rotator, *Nucl. Phys. A* 637(2), 201 (1998)
46. A. A. Raduta, R. Budaca, and C. M. Raduta, Semiclassical description of a triaxial rigid rotor, *Phys. Rev. C* 76(6), 064309 (2007)
47. O. von Roos, Position-dependent effective masses in semiconductor theory, *Phys. Rev. B* 27(12), 7547 (1983)
48. Q. B. Chen, S. Q. Zhang, P. W. Zhao, and J. Meng, Collective Hamiltonian for wobbling modes, *Phys. Rev. C* 90(4), 044306 (2014)
49. Q. B. Chen, S. Q. Zhang, and J. Meng, Wobbling motion in ^{135}Pr within a collective Hamiltonian, *Phys. Rev. C* 94(5), 054308 (2016)
50. Q. B. Chen, K. Starosta, and T. Koike, Three-level mixing model for nuclear chiral rotation: Role of the planar component, *Phys. Rev. C* 97, 041303(R) (2018)
51. K. Starosta, T. Koike, C. J. Chiara, D. B. Fossan, and D. R. LaFosse, Chirality in odd–odd triaxial nuclei, *Nucl. Phys. A.* 682(1–4), 375 (2001)
52. J. Timár, K. Starosta, I. Kuti, D. Sohler, D. B. Fossan, T. Koike, E. S. Paul, A. J. Boston, H. J. Chantler, M. Descovich, R. M. Clark, M. Cromaz, P. Fallon, I. Y. Lee, A. O. Macchiavelli, C. J. Chiara, R. Wadsworth, A. A. Hecht, D. Almehed, and S. Frauendorf, Medium- and high-spin band structure of the chiral-candidate nucleus ^{134}Pr, *Phys. Rev. C* 84(4), 044302 (2011)
53. K. Y. Ma, J. B. Lu, Z. Zhang, J. Q. Liu, D. Yang, Y. M. Liu, X. Xu, X. Y. Li, Y. Z. Liu, X. G. Wu, Y. Zheng, and C. B. Li, Candidate chiral doublet bands in ^{138}Pm, *Phys. Rev. C* 97(1), 014305 (2018)
54. C. M. Petrache, D. Bazzacco, S. Lunardi, C. Rossi Alvarez, G. de Angelis, M. De Poli, D. Bucurescu, C. A. Ur, P. B. Semmes, and R. Wyss, Rotational bands in the doubly odd nucleus ^{134}Pr, *Nucl. Phys. A* 597(1), 106 (1996)
55. K. Starosta, C. J. Chiara, D. B. Fossan, T. Koike, T. T. S. Kuo, D. R. LaFosse, S. G. Rohozinski, Ch. Droste, T. Morek, and J. Srebrny, Role of chirality in angular momentum coupling for $A \sim 130$ odd–odd triaxial nuclei: ^{132}La, *Phys. Rev. C* 65(4), 044328 (2002)
56. P. Siwach, P. Arumugam, L. S. Ferreira, and E. Maglione, Chirality in ^{136,138}Pm, *Phys. Lett. B* 811, 135937 (2020)
57. P. Möller, A. J. Sierk, T. Ichikawa, and H. Sagawa, Nuclear ground-state masses and deformations: FRDM(2012), *At. Data Nucl. Data Tables* 109–110, 1 (2016)
58. R. Budaca, Tilted-axis wobbling in odd-mass nuclei, *Phys. Rev. C* 97(2), 024302 (2018)
59. R. Budaca, Reconciliation of wobbling motion with rotational alignment in odd mass nuclei, *Phys. Rev. C* 103(4), 044312 (2021)
60. B. F. Lv, C. M. Petrache, R. Budaca, A. Astier, K. K. Zheng, P. Greenlees, H. Badran, T. Calverley, D. M. Cox, T. Grahn, J. Hilton, R. Julin, S. Juutinen, J. Konki, J. Pakarinen, P. Papadakis, J. Partanen, P. Rahkila, P. Ruotsalainen, M. Sandzelius, J. Saren, C. Scholey, J. Sorri, S. Stolze, J. Uusitalo, B. Cederwall, A. Ertoprak, H. Liu, S. Guo, J. G. Wang, H. J. Ong, X. H. Zhou, Z. Y. Sun, I. Kuti, J. Timár, A. Tucholski, J. Srebrny, and C. Andreoiu, Experimental evidence for transverse wobbling bands in ^{136}Nd, *Phys. Rev. C* 105(3), 034302 (2022)
61. R. Budaca and C. M. Petrache, Beyond the harmonic approximation description of wobbling excitations in even–even nuclei with frozen alignments, *Phys. Rev. C* 106(1), 014313 (2022)